Supplementary Information for

General synthesis of high-entropy alloy and ceramic nanoparticles in nanoseconds

Bing Wang[1,2,4,7], Cheng Wang[3], Xiwen Yu[3], Yuan Cao[1], Linfeng Gao[3], Wenjun Luo [1,3,4,7], Congping Wu[1,7], Yingfang Yao[1,3,4,7*], Zhiqun Lin[2*], Zhigang Zou[1,3,4,5,6,7*].

Correspondence to: zgzou@nju.edu.cn (Z. Z.); zhiqun.lin@mse.gatech.edu (Z. L.); yaoyingfang@nju.edu.cn (Y. Y.).

Section S1 Laser Parameters

A pulsed fiber laser (SLT-PTM-100, Jiangsu Yanchang Sunlaite new engergy Co.,Ltd, China) with the fundamental wavelength of 1064 nm, energy of 14.15J/cm^2 and pulse length of 5 ns was used for the ablation. The laser was operated at a repetition rate of 20 KHz with the travelling speed of 600 mm/s. A Gaussian laser beam with the peak power of 20 kW was focused by a set of optical components and supplied at normal incidence to the surface of the substrate, as shown in Fig. 1c in the main text. Fig. S1 depicts the laser scanning strategy. The laser scanning path was set to be back and forth along the x-axis and forth along the y-axis, which involves two kinds of overlap rates (i.e. scan line overlap and spot overlap) 1. Based on the scanning speed and the size of the laser spot (30 μm), we calculated the scan line overlap (O_L) and spot overlap (O_S) of 0 μm. Namely, the laser spots continuously hit the substrate surface without overlapping. For each point on the substrate, it received only one laser spot (5 ns) for a laser scanning cycle.

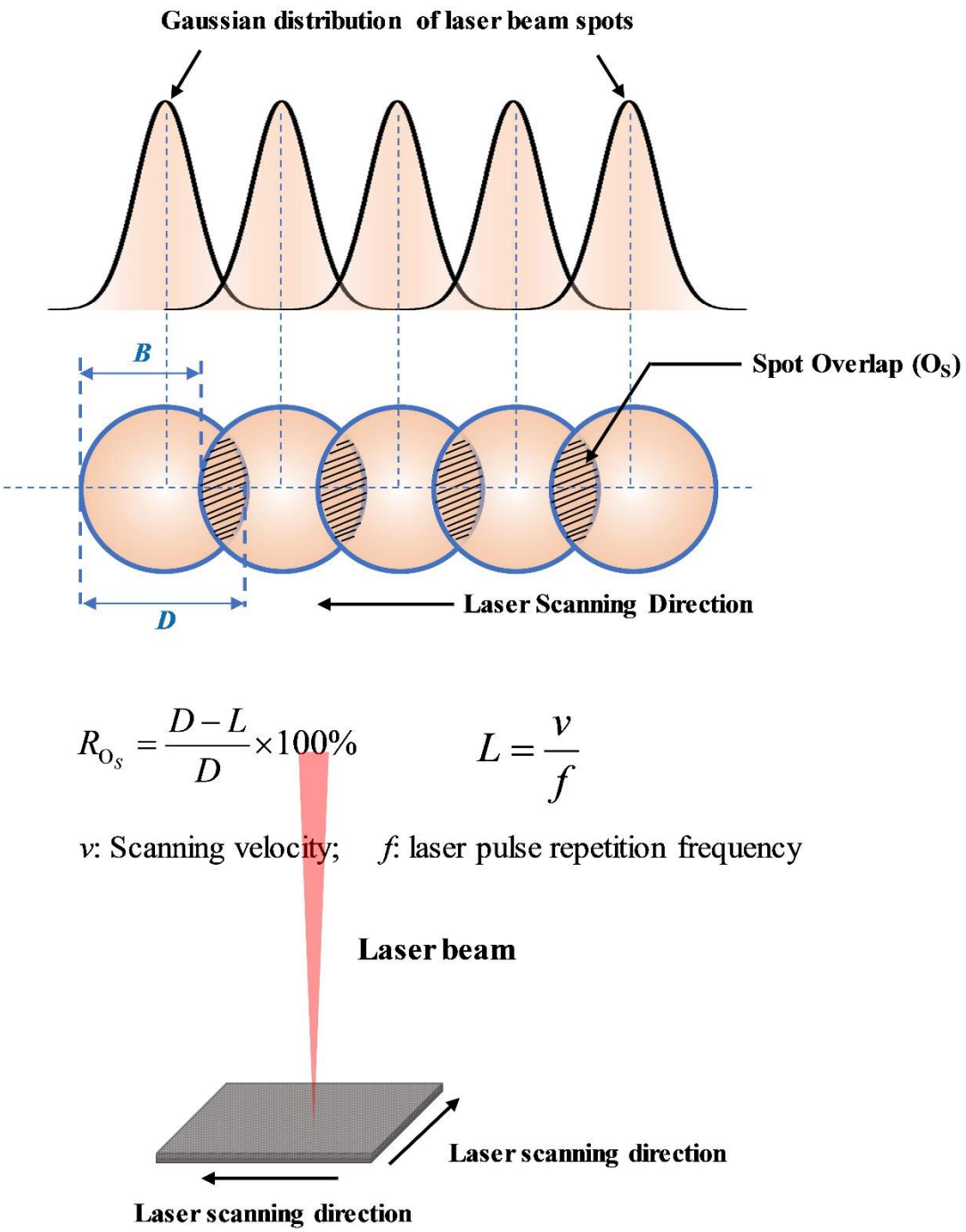

Fig. S1 (a) Ablated line with circular laser footprint, and **(b)** laser scanning direction strategy.

Section S2 Configurational Entropy of Mixing

Total mixing entropy has four contributions including configurational entropy, atomic vibration, electronic randomness, and magnetic dipole[1]. Configurational entropy is dominant over other three contributions. According to the Boltzmann's hypothesis, the configurational mixing entropy (ΔS_{mix}) can be expressed as:

$$\Delta S_{mix} = -R\sum_{i=1}^{n} c_i \ln c_i$$

where, R is gas constant (8.314 J/K mol), n is the number of principal elements, c_i is mole fraction of composition i. ΔS_{mix} will reach the maximum when the alloy is of equi-atomic ratio. It is 0.69R, 1.10R, 1.61R, respectively, for two, three and five principal elements mixed in equimolar ratio (Fig. S2). In a broad sense, 1.5R is large enough to compete with most strong bonding energies of unlike atomic pairs at high temperatures, and it is used as a border line between HEAs and medium-entropy alloys[2]. As the increase growth rate of ΔS_{mix} after a 9-element alloy is slowing down, HEAs with 5 to 9 constituent elements is suggested in practical application[2,3]. More elements will not benefit from high entropy yet increasing the complexity in material system.

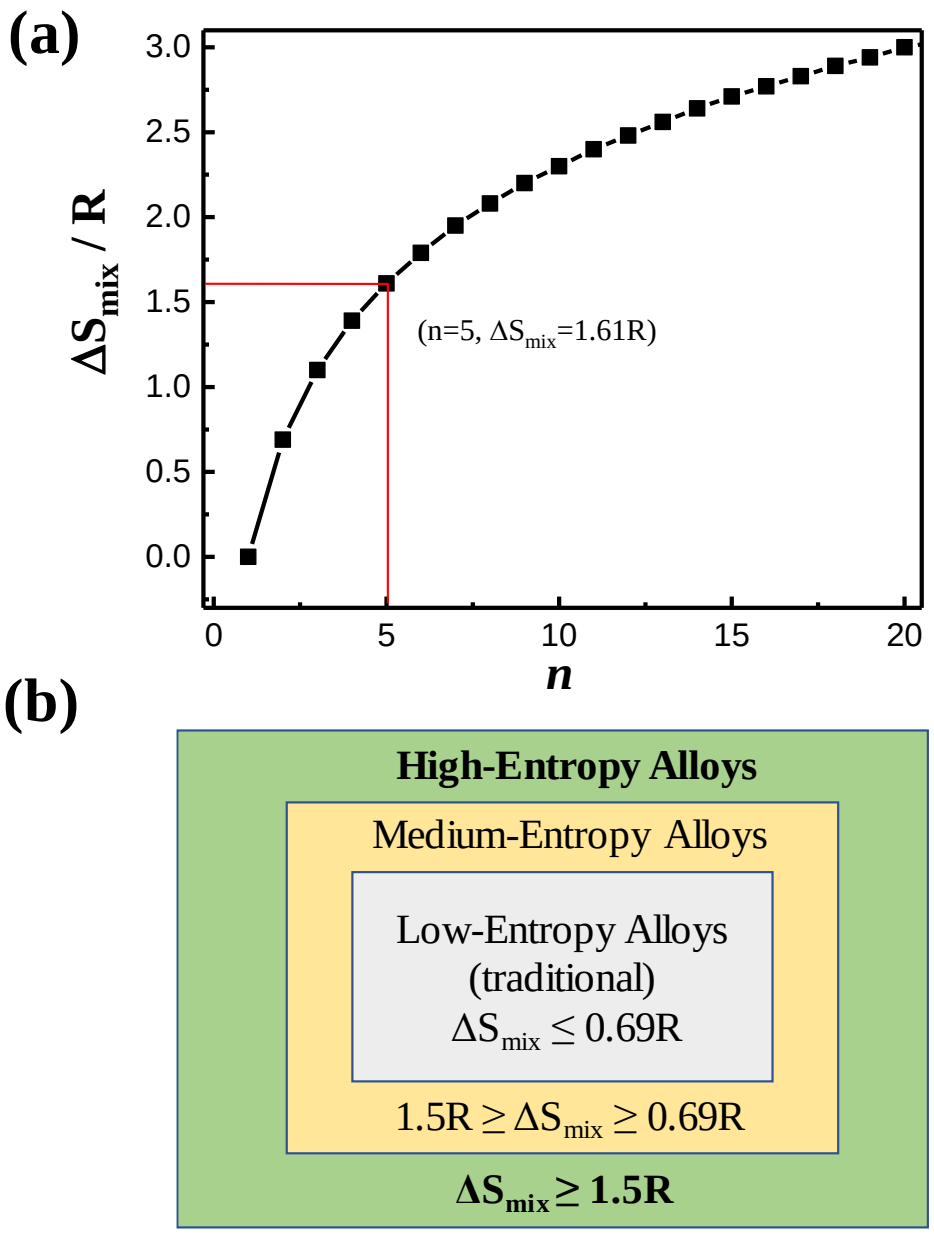

Fig. S2 (a) The configurational entropy of mixing as a function of the number of elements for equimolar alloys. **(b)** Alloy definitions based on configurational entropy.

Section S3 Photothermal Evaporation and Coulomb Explosion Mechanisms

Generally, two major models can interpret a laser-induced nanofabrication, including photothermal evaporation and Coulomb explosion mechanisms[4]. A laser with high irradiance and ultra-short pulse widths, such as femtosecond pulsed-laser, favors the production of NPs through Coulomb explosion because the electron temperatures ($T_{electron}$) can easily reach the threshold of the Coulomb explosion. Under femisecond pulses, $T_{electron}$ in metal atoms rises rapidly in femoseconds to reach a value above the threshold of Columb Explosion (Fig. S3a).[4] The energy in the electrons is then transferred to lattices via electron−phonon coupling, resulting in a rise of lattice temperature ($T_{lattice}$) within picoseconds. Subsequently, $T_{electron}$ and $T_{lattice}$ reach their thermal equilibrium through heat exchange with the surrounding hexane.In contrast, a milder laser irradiation such as nanosecond pulsed-laser used in this work contributes to photothermal pathways as the temperature provided is insufficient to reach the temperature for Coulomb explosion but can go above the melting or boiling points of metals[5]. Under nanosecond pulsed laser, $T_{electron}$ and $T_{lattice}$ increase almost synchronously(Fig. S3b). The energy deposited into the electrons and lattice is delivered into the hexane. Due to this energy transfer, the liquid at the contact zone with substrate undergoes a phase transition that causes the formation of a thin layer of vapor. The vapor layer expands rapidly to form a vapor bubble.[6] A steep rise in $T_{lattice}$ can be observed at the onset of bubble generation. The two flat temperature curve in $T_{lattice}$ (Fig. S3b) means no temperature rise occurs due to the consumption of the melting or evaporation enthalpy[4].

In our work, we mainly used the model of photothermal evaporation to understand the formation mechanism of HEA NPs.

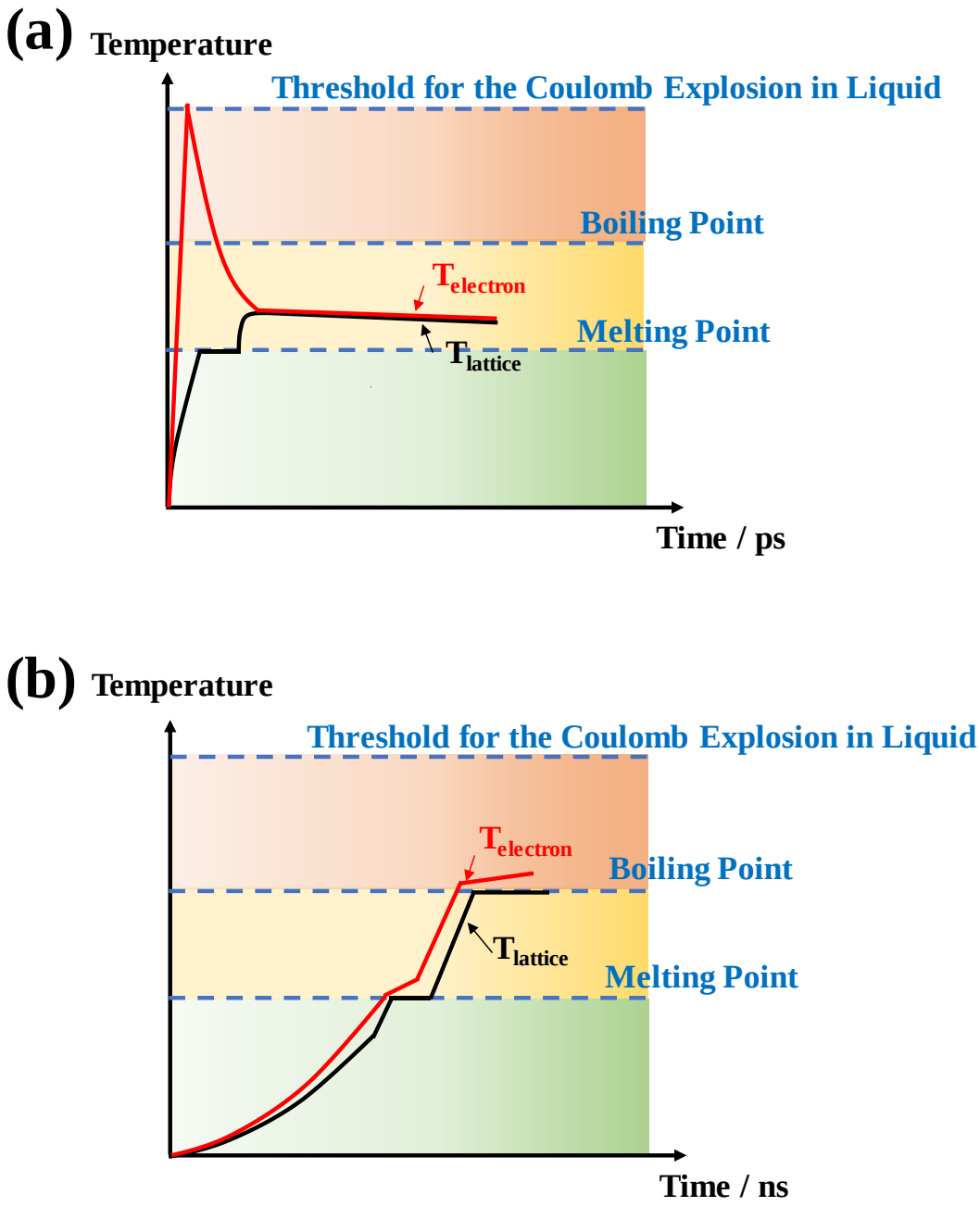

Fig. S3 Time dependent temperature evolution of electrons, $T_{electron}$ (red curve); lattice, $T_{lattice}$ (black curve) for an HEA sphere interacting with a (a) femtosecond and (b) nanosecond laser pulse[4].

Section S4 Thermodynamically forbidden compositions

Despite different properties of metallic elements (table S1), LSA method allows the synthesis of HEA NPs with thermodynamically forbidden compositions (Fig. S4) and uniform elemental distributions.

According to the Hume-Rothery rules, there should meet four constraints to form solid solution[7]: (1) the difference of the atomic radius for the solute elements must be within 15%, (2) the chemical valence of the solute elements must differ by no more than one, (3) the crystal structure must be the same, and (4) the electronegativities must be nearly equal. As shown in Figure S4, it is clearly seen that these conditions are not fulfilled among many pairs of elements. This indicates that the Hume-Rothery rules do not apply to the synthesis of HEAs by LSA method.

Table S1 The physical properties of eleven metallic elements employed in this work. MT: melting temperature; BT: boiling temperature; ET: electron temperature; AR: atomic radius; EN: electronegativity; CV: chemical valence; RP: reduction potential (vs NHE).

	Pt	**Pd**	**Au**	**Ir**	**Fe**	**Co**	**Ni**	**Cu**	**Sn**	**Cr**	**Zn**
MT / K	2045	1825	1335	2683	1808	1768	1726	1356	505	1857	420
BT / K	4100	3413	3239	4403	3023	3143	3005	2853	2963	2672	907
AR / pm	139	138	144	136	127	126	125	128	141	127	139
EN	2.26	2.20	2.54	2.20	1.83	1.89	1.91	1.90	1.96	1.66	1.65
CV	+4	+2	+3	+4	+3	+2	+2	+2	+4	+3	+2
RP/ V	0.755	0.951	1.002	0.77	-0.037	-0.280	-0.257	0.342	-0.137	-0.740	-0.763

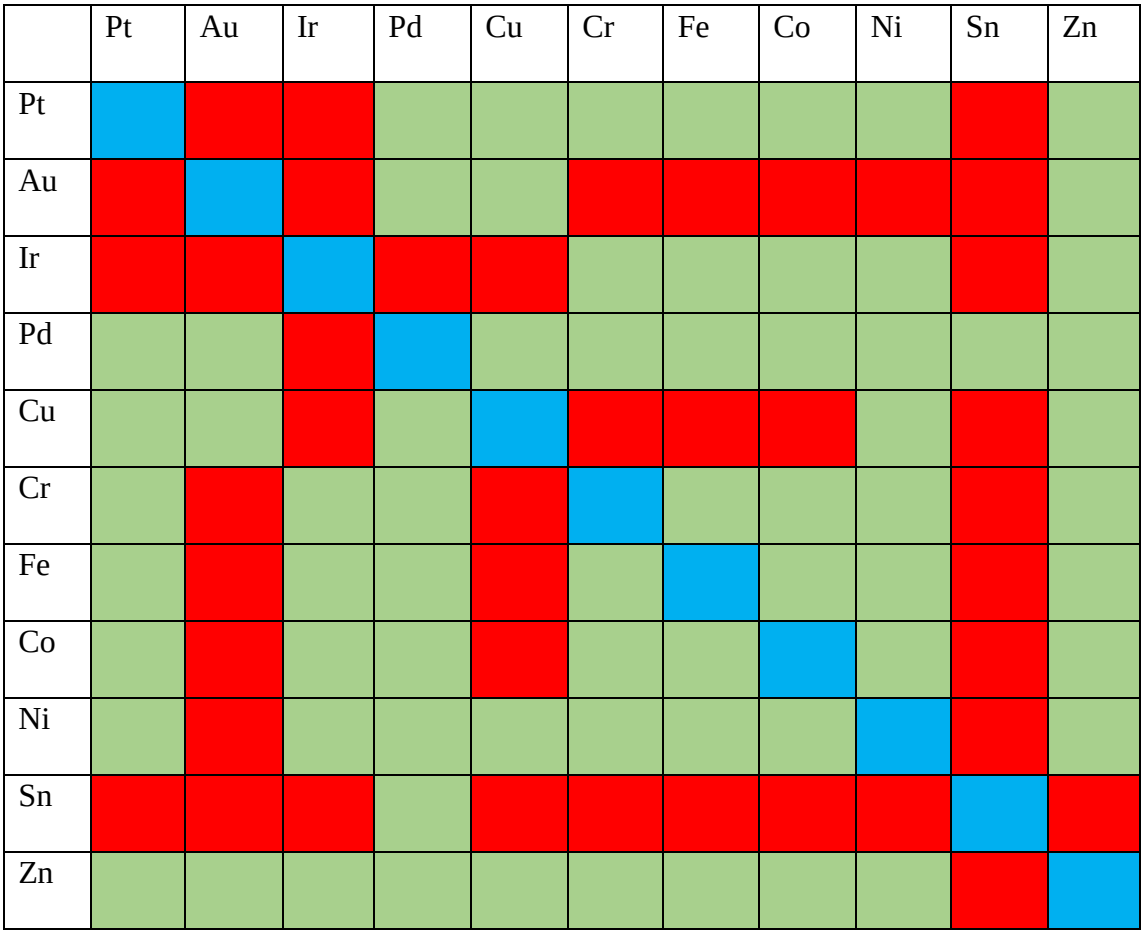

Fig. S4 The miscibility maps of binary elementary combinations[8]. The red and green rectangles indicate immiscible and miscible combinations, respectively. The blue rectangles represent the boundary of alloys consisting of dissimilar elements.

Section S5 Regulation of the HEA NPs size and distribution

The Extended Data Fig. 3a-3c shows micrographs and the corresponding size distributions of the HEA NPs with Pt, Au, Pd, Cu, Cr, Sn elements produced under different laser scanning time. By controlling laser scanning cycles of 1, 5, 10, 20 times corresponding with interaction time of 5, 25, 50, 100 ns for each point on the substrate, the average diameters of the HEA NPs were measured to be 11.0±4.6, 28.9±16.0, 36.8±18.4 and 56.2±20.7 nm, respectively. The NPs shift to larger sizes with broader distribution as scanning cycles increase. At the first laser scanning, HEA NPs form by direct HEA nucleation from metal precursors (see Fig. 2a in main text). When these NPs are exposed under next laser pulse, two processes are involved[9]. Apart from the direct HEA nucleation from metal salts, the other process is that the existing NPs continuously enlarge by fusing with next incoming species (see the Extended Data Fig. 3d). Hence, a broader size distribution of HEA NPs is observed under repeated laser scanning. The variations of the NP size and distribution further prove that the LSA mechanism in this work follows the model of photothermal evaporation rather than Coulombic explosion because the latter would generate smaller particles with the increase of laser scanning cycles[10,11]. We further ablated the precursors at hexane temperatures of -196 and 0 ^{0}C achieved by liquid nitrogen and ice treatments, respectively, to control the size and distribution of HEAs. A lower temperature causes generation of smaller cavitation bubbles[12] (see Panel IV in Fig. 2a of main text), which is favorable for the formation of smaller NPs and more uniform size distribution (see the Extended Data Fig.4a) with more controllable stoichiometric ratios (see the Extended Data Fig.4d).

The bubble radius enables estimating the temperature (T) and pressure (P) of the vapor inside the bubble with the van der Waals state equation[13]:

$$P = (P_\infty + \frac{2\sigma}{R})\left(\frac{R_\infty - h^3}{R^3 - h^3}\right)$$

$$T = T_\infty \left(\frac{R_\infty - h^3}{R^3 - h^3}\right)^{\gamma - 1}$$

P_∞ and T_∞ are pressure and temperature of the liquid (hexane), R is the radius determined as a function of the delay time from the laser pulse, R_∞ is the radius at which pressure inside the bubble corresponds to the liquid pressure, σ is the surface tension of the liquid, h is the actual radius which can be determined by $R_\infty/9.174$, γ with the value of 1.22 is the polytropic exponent of the gas within the bubble. The lower hexane temperature (T_∞) and the smaller bubble radius (R_∞, observed during LSA process) demonstrate a lower temperature and pressure environment inside the cavitation bubbles. Such a bubble environment reduced metal evaporation loss and achieved better compositional control, as shown in Extended Data Fig. 4d. In contrast, a higher hexane temperature and a larger bubble sizes reveal higher temperature and pressure inside the cavitation bubbles, which results in a wider particle size distribution and a greater disturbance in the composition ratio of the final NPs due to more metal loss. Thus, more uniform and smaller NPs indicated improved compositional distribution.

Additionally, the FCC structure of the PtAuCuFeCo still maintains (see Extended Data Fig. 4e) after ablation in -196 ^{0}C, implying that the cooling rate is not high enough to form metallic glassy phase.

Section S6 Electrocatalytic activity of HEA NPs

Applied as the electrocatalyst for water splitting, HEA NPs of PtIrCuNiCr achieved an overpotential of 185 mV @ 10mA cm^{-2}, which was among the best activities currently (Table S2). Due to the atomic size mismatch of different metals, HEA NPs of PtIrCuNiCr exhibit severe lattice distortion compared with traditional NPs such as the reported catalysts in Table S2. The lattice distortion of HEA caused lattice strain[14], and further induced a thermodynamically nonequilibrium state. Such a state contributes to a higher potential energy, thus decreasing energy barrier during catalytic reactions and improving catalytic performance.

Surface charge density of catalysts is another important factor to influence catalytic performance. For monometallic NPs, the surface charge density is essentially the same due to the same surface atoms. As for HEA NPs of PtIrCuNiCr, charge transfer between different surface atoms occurs due to the distinct work functions of Pt (5.65 eV), Ir (5.27 eV), Cu (4.65 eV), Ni (5.12 eV), Cr (4.50 eV), resulting in alternative accumulation and scarcity of electrons across the surface of PtIrCuNiCr. The change of local charge density creates more active sites[15] to adsorb and active water molecules during electrocatalytic reactions, which thus enhances the electrocatalytic performance of PtIrCuNiCr HEA NPs.

Table S2 Comparison of electrocatalytic performance with the most recently reported bifunctional catalysts for overall water splitting. $\eta_{10,\ Overall}$ and $\eta_{100,\ Overall}$ correspond to the overpotential of OER to achieve a current density of 10 and 100 mA cm^{-2}, respectively. (MOF: Metal–Organic Frameworks; LDH: Layered Double Hydroxide; SWNTs: Single-Walled Carbon Nanotubes; NCNFs: Nitrogen-Doped Carbon Nanofibers;)

Bifunctional catalyst	**Electrolytes**	**$\eta_{10,\ Overall}$ (mV)**	**$\eta_{100,\ Overall}$ (mV)**	**Source**
Ni_3N	1 M KOH	280	—	[16]
Co-Ru-MoS_2	1 M KOH	310	—	[17]
Ir @Co	1 M KOH	315	—	[18]
Co@Ir/MOF	1 M KOH	270	—	[19]
Fe-Ni_3S_2	1 M KOH	310	460	[20]
Pt-CoS_2	1 M KOH	320	—	[21]
RuO_2/NiO	1 M KOH	270	—	[22]
Rh/SWNTs	1 M KOH	360	—	[23]
RuNi-NCNFs	1 M KOH	334	—	[24]
Fe/Co/Ni@RuO_2	1 M KOH	312	—	[25]
Co@Pt/ C	1 M KOH	310	—	[26]
$PtO_aPdO_bNPs@Ti_3C_2T_x$	1 M KOH	300	520	[27]
Ru/$Ni(OH)_2$	1 M KOH	270	—	[28]
Ru-NiFe-P	1 M KOH	240	430	[29]
NiFe LDH@NiCoP	1 M KOH	340	680	[30]
MoS_2/NiFe-LDH	1 M KOH	340	—	[31]
Se^{-}(NiCo)S/OH	1 M KOH	370	850	[32]
PtIrCuNiCr-graphene	1 M KOH	185	300	This work

References

1 Fultz, B. Vibrational thermodynamics of materials. Prog Mater Sci **55**, 247-352, doi:10.1016/j.pmatsci.2009.05.002 (2010).

2 Yeh, J. W. Alloy design strategies and future trends in high-entropy alloys. Jom-Us **65**, 1759-1771, doi:10.1007/s11837-013-0761-6 (2013).

3 Yeh, J. W. Recent progress in high-entropy alloys. Ann Chim-Sci Mat **31**, 633-648, doi:10.3166/acsm.31.633-648 (2006).

4 Werner, D. & Hashimoto, S. Improved working model for interpreting the excitation wavelength- and fluence-dependent response in pulsed laser-induced size reduction of aqueous gold nanoparticles. J Phys Chem C **115**, 5063-5072, doi:10.1021/jp109255g (2011).

5 Liu, D. L. et al. Rapid synthesis of monodisperse Au nanospheres through a laser irradiation-induced shape conversion, self-assembly and their electromagnetic coupling SERS enhancement. Sci Rep-Uk **5**, doi:10.1038/srep07686 (2015).

6 Dell'Aglio, M., Gaudiuso, R., De Pascale, O. & De Giacomo, A. Mechanisms and processes of pulsed laser ablation in liquids during nanoparticle production. Appl Surf Sci **348**, 4-9, doi:10.1016/j.apsusc.2015.01.082 (2015).

7 Tong, C. J. et al. Microstructure characterization of AlxCoCrCuFeNi high-entropy alloy system with multiprincipal elements. Metall Mater Trans A **36a**, 881-893, doi:10.1007/s11661-005-0283-0 (2005).

8 Zhang, R. F. et al. An informatics guided classification of miscible and immiscible binary alloy systems. Sci Rep-Uk **7**, doi:10.1038/s41598-017-09704-1 (2017).

9 Xiao, J., Liu, P., Wang, C. X. & Yang, G. W. External field-assisted laser ablation in liquid: An efficient strategy for nanocrystal synthesis and nanostructure assembly. Prog Mater Sci **87**, 140-220, doi:10.1016/j.pmatsci.2017.02.004 (2017).

10 Jeon, J. W. et al. The effect of laser pulse widths on laser-Ag nanoparticle interaction: Femto- to nanosecond lasers. Appl Sci-Basel **8**, doi:10.3390/app8010112 (2018).

11 Hashimoto, S., Werner, D. & Uwada, T. Studies on the interaction of pulsed lasers with plasmonic gold nanoparticles toward light manipulation, heat management, and nanofabrication. J Photoch Photobio C **13**, 28-54, doi:10.1016/j.jphotochemrev.2012.01.001 (2012).

12 Menendez-Manjon, A., Chichkov, B. N. & Barcikowski, S. Influence of water temperature on the hydrodynamic diameter of gold nanoparticles from laser ablation. J Phys Chem C **114**, 2499-2504, doi:10.1021/jp909897v (2010).

13 De Giacomo, A. et al. Cavitation dynamics of laser ablation of bulk and wire-shaped metals in water during nanoparticles production. Phys Chem Chem Phys **15**, 3083-3092, doi:10.1039/c2cp42649h (2013).

14 Lv, Z. Y. et al. Development of a novel high-entropy alloy with eminent efficiency of degrading azo dye solutions. Sci Rep-Uk **6**, doi:10.1038/srep34213 (2016).

15 Du, X. C. et al. Modulating electronic structures of inorganic nanomaterials for efficient electrocatalytic water splitting. Angew Chem Int Edit **58**, 4484-4502, doi:10.1002/anie.201810104 (2019).

16 Yan, H. J. et al. Anion-modulated HER and OER activities of 3D Ni-V-based interstitial compound heterojunctions for high-efficiency and stable overall water splitting. Adv Mater **31**, doi:10.1002/adma.201901174 (2019).

17 Kwon, I. S. et al. Ruthenium nanoparticles on cobalt-doped 1T ' phase MoS_2 nanosheets for overall water splitting. Small **16**, doi:10.1002/smll.202000081 (2020).
18 Lai, W. H. et al. General pi-electron-assisted strategy for Ir, Pt, Ru, Pd, Fe, Ni single-atom electrocatalysts with bifunctional active sites for highly efficient water splitting. Angew Chem Int Edit **58**, 11868-11873, doi:10.1002/anie.201904614 (2019).
19 Li, D. L. et al. Total water splitting catalyzed by Co@Ir Core-Shell nanoparticles encapsulated in nitrogen-doped porous carbon derived from metal organic frameworks. Acs Sustain Chem Eng **6**, 5105-5114, doi:10.1021/acssuschemeng.7b04777 (2018).
20 Zhang, G. et al. Enhanced catalysis of electrochemical overall water splitting in alkaline media by Fe doping in Ni_3S_2 nanosheet arrays. Acs Catal **8**, 5431-+, doi:10.1021/acscatal.8b00413 (2018).
21 Han, X. P. et al. Ultrafine Pt nanoparticle-decorated pyrite-type CoS_2 nanosheet arrays coated on carbon cloth as a bifunctional electrode for overall water splitting. Adv Energy Mater **8**, doi:10.1002/aenm.201800935 (2018).
22 Liu, J. L. et al. NiO as a bifunctional promoter for RuO_2 toward superior overall water splitting. Small **14**, doi:10.1002/smll.201704073 (2018).
23 Zhang, W. Q. et al. Single-walled carbon nanotube induced optimized electron polarization of rhodium nanocrystals to develop an interface catalyst for highly efficient electrocatalysis. Acs Catal **8**, 8092-8099, doi:10.1021/acscatal.8b02016 (2018).
24 Li, M. X. et al. RuNi nanoparticles embedded in N-doped carbon nanofibers as a robust bifunctional catalyst for efficient overall water splitting. Adv Sci **7**, doi:10.1002/advs.201901833 (2020).
25 Wang, J. et al. Transition metal-doped ultrathin RuO_2 networked nanowires for efficient overall water splitting across a broad pH range. J Mater Chem A **7**, 6411-6416, doi:10.1039/c9ta00598f (2019).
26 Zhang, H. et al. Open hollow Co-Pt clusters embedded in carbon nanoflake arrays for highly efficient alkaline water splitting. J Mater Chem A **6**, 20214-20223, doi:10.1039/c8ta07101b (2018).
27 Cui, B. B. et al. Solution-plasma-assisted bimetallic oxide alloy nanoparticles of Pt and Pd embedded within two-dimensional $Ti_3C_2T_X$ nanosheets as highly active electrocatalysts for overall water splitting. Acs Appl Mater Inter **10**, 23858-23873, doi:10.1021/acsami.8b06568 (2018).
28 Chen, Q. Q., Yang, X., Hou, C. C., Li, K. & Chen, Y. Inlay of ultrafine Ru nanoparticles into a self-supported Ni(OH)(2) nanoarray for hydrogen evolution with low overpotential and enhanced kinetics. J Mater Chem A **7**, 11062-11068, doi:10.1039/c9ta02451d (2019).
29 Qu, M. J. et al. Regulating electron density of NiFe-P nanosheets electrocatalysts by a trifle of Ru for high-efficient overall water splitting. Appl Catal B-Environ **263**, doi:10.1016/j.apcatb.2019.118324 (2020).
30 Zhang, H. J. et al. Bifunctional heterostructure assembly of NiFe LDH nanosheets on NiCoP nanowires for highly efficient and stable overall water splitting. Adv Funct Mater **28**, doi:10.1002/adfm.201706847 (2018).
31 Xiong, P. et al. Interface modulation of two-dimensional superlattices for efficient overall water splitting. Nano Lett **19**, 4518-4526, doi:10.1021/acs.nanolett.9b01329 (2019).
32 Hu, C. L. et al. Synergism of geometric construction and electronic regulation: 3D Se-$(NiCo)S_x/(OH)_x$ nanosheets for highly efficient overall water splitting. Adv Mater **30**, doi:10.1002/adma.201705538 (2018).